ELECTROCHEMISTRY

A smart risk-responding polymer membrane for safer batteries

Ying Zhang[1], Le Yu[2], Xu-Dong Zhang[1], Ya-Hui Wang[1], Chunpeng Yang[3], Xiaolong Liu[1], Wen-Peng Wang[1], Yu Zhang[1], Xue-Ting Li[1], Ge Li[4], Sen Xin[1,5]*, Yu-Guo Guo[1,5]*, Chunli Bai[1,5]

Safety concerns related to the abuse operation and thermal runaway are impeding the large-scale employment of high-energy-density rechargeable lithium batteries. Here, we report that by incorporating phosphorus-contained functional groups into a hydrocarbon-based polymer, a smart risk-responding polymer is prepared for effective mitigation of battery thermal runaway. At room temperature, the polymer is (electro)chemically compatible with electrodes, ensuring the stable battery operation. Upon thermal accumulation, the phosphorus-containing radicals spontaneously dissociate from the polymer skeleton and scavenge hydrogen and hydroxyl radicals to terminate the exothermic chain reaction, suppressing thermal generation at an early stage. With the smart risk-responding strategy, we demonstrate extending the time before thermal runaway for a 1.8-Ah Li-ion pouch cell by 100% (~9 hours) compared with common cells, creating a critical time window for safety management. The temperature-triggered automatic safety-responding strategy will improve high-energy-density battery tolerance against thermal abuse risk and pave the way to safer rechargeable batteries.

INTRODUCTION

The energy demand of emerging storage applications including portable electronic devices, electric vehicles, and stationary energy storage is raising the requirement for energy density of rechargeable batteries (*1*–*9*). The pursuit of high energy density imposes urgent challenges to battery safety (Fig. 1A) (*10*–*12*). The commonly used polymer separators, which mainly consist of polypropylene (PP) and polyethylene (PE), easily shrink and melt down at elevated temperatures (PP melts at ~165°C and PE melts at ~140°C), causing internal short circuit (*13*). At the higher temperature, organic electrolytes decompose and release enormous highly reactive free radicals (e.g., $H^{\bullet}$ and $HO^{\bullet}$) and strong Lewis acid phosphorus pentafluoride (PF_5) (Fig. 1B) (*14*, *15*). When the decomposed products meet with the released oxygen from the cathode phase transition at around 200°C (*16*), the generated heat increases exponentially, leading to catastrophic thermal runaway. Moreover, the polymer separators and the organic liquid electrolytes are highly flammable. The unstable material and chemistry of the battery components account for a growing number of thermal runaway incidents including overheating, smoke, fire, and even explosion. Safety remains the prerequisite for the development of rechargeable batteries with high energy densities.

In the past decades, various attempts have been made to enhance battery safety. One direction is to develop inherently safe solid inorganic electrolytes (*7*, *17*). However, so far, the electrochemical performance of solid-state batteries is far from satisfactory compared with current Li-ion batteries using liquid electrolytes, especially at room temperature. Another direction is to use aqueous electrolytes instead of organic electrolytes, but the aqueous batteries deliver much lower energy densities than nonaqueous Li-ion batteries (*18*, *19*). A more feasible strategy is to add flame-retardant additives or cosolvents in organic electrolytes to resist the combustion of organic electrolytes. Halogenated or phosphorus-based compounds are found effective to improve battery safety by capturing and consuming active free radicals (*20*). However, halogenated compounds generate toxic and corrosive hydrogen halide gases during pyrolysis (*21*–*23*). Most phosphorus-based solvents, such as triphenyl phosphate (*24*), triethyl phosphate (*25*), and tributyl phosphate (*26*), are electrochemically unfavorable with limited operating voltages and poor passivation with anodes (graphite and Li), limiting the life span of the batteries (Fig. 1C) (*27*, *28*). It remains a daunting task to mitigate the thermal runaway risk of high-energy-density batteries while maintaining desirable electrochemical performance (energy density and life span).

In this work, we propose a smart risk-responding (SRR) strategy for high-energy and high-safety batteries, i.e., using a polymer membrane that enables high performance at room temperature and automatically releases flame-retardant radicals under thermal abuse conditions to ensure safety. As a proof of concept, we use trimethylolpropane ethoxylate triacrylate (TMPETA) grafted with diethyl allylphosphonate (DEAP) monomers in a poly(vinylidene fluoride-co-hexafluoropropylene) (PVDF-HFP) membrane, denoted as TPF, as an SRR membrane. In stark contrast with the previously reported P-containing additives or cosolvents, the DEAP is covalently bonded with the polymer skeleton and does not release electrochemically unfavorable P-containing molecules

[1]CAS Key Laboratory of Molecular Nanostructure and Nanotechnology, CAS Research/Education Center for Excellence in Molecular Sciences, Beijing National Laboratory for Molecular Sciences (BNLMS), Institute of Chemistry, Chinese Academy of Sciences (CAS), Beijing 100190, P. R. China. [2]Key Laboratory of Synthetic and Natural Functional Molecule of the Ministry of Education, College of Chemistry & Materials Science, Northwest University, Xi'an, Shaanxi 710127, P. R. China. [3]School of Chemical Engineering and Technology, Tianjin University, Tianjin 300072, P. R. China. [4]Beijing IAmetal New Energy Technology Co. Ltd., Beijing 100190, P. R. China. [5]University of Chinese Academy of Sciences, Beijing 100049, P. R. China.
*Corresponding author. Email: xinsen08@iccas.ac.cn (S.X.); ygguo@iccas.ac.cn (Y.-G.G.)

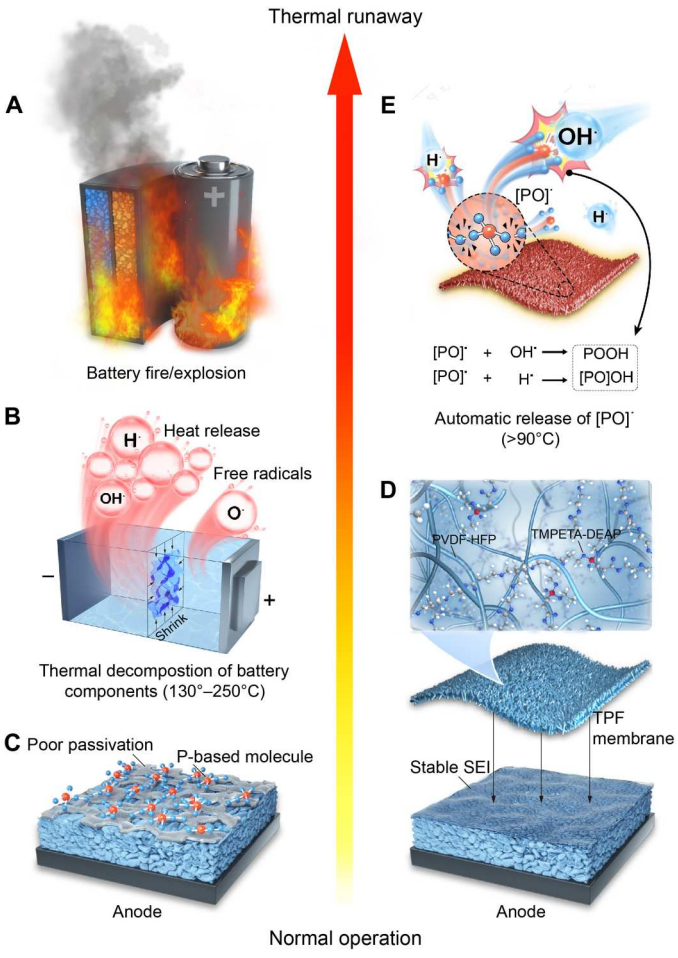

Fig. 1. Mitigation of battery thermal runaway by the SRR strategy. (**A**) Thermal runaway incidents of rechargeable Li-ion batteries, including overheating, smoking, fires, and even explosions. (**B**) Thermal decomposition issues (separator meltdown and electrolyte/cathode breakdown) in a thermal abuse state, releasing a large quantity of highly reactive free radicals (e.g., H•, HO• and O•), causing severe thermal accumulation and final thermal runaway. (**C**) Schematic of application limitations of P-based flame-retardant additives or cosolvents for Li-ion batteries, including poor passivation at the anode-electrolyte interface and limited cyclic performance. (**D**) Application superiorities of the TPF membrane for Li-ion batteries at a normal operation state. The TPF membrane with covalently linked diethyl allylphosphonate (DEAP) functional groups substantially enhances the electrochemical stability with anodes and enables a long-term cycle life. (**E**) Graphical illustration of mitigation of thermal runaway in batteries by the TPF membrane when the battery temperature increases beyond 90°C. P-containing free radicals produced from TPF pyrolysis interfere with the exothermic process by radicals quenching, which mitigates thermal runaway to bring enhanced battery safety. PVDF-HFP, poly(vinylidene fluoride-co-hexafluoropropylene); TMPETA, trimethylolpropane ethoxylate triacrylate.

during normal battery operation (Fig. 1D). With the TPF polymer, a SiO_x graphite (SiO_x-G)//NCM811 battery delivers a high areal capacity of 3.9 mAh cm^{-2}, an average Coulombic efficiency of 99.6%, and a capacity retention of 91.4% after 100 cycles. If the battery temperature elevates to 90°C in a thermal abuse state, the TPF polymer automatically releases P-containing free radicals to suppress the exothermic chain reaction, markedly postponing the occurrence of fatal thermal runaway (Fig. 1E). Thus, the SRR membrane realizes electrochemical compatibility with both the high-voltage cathodes and common anodes (graphite-based or metallic Li anodes) for high-energy-density batteries while spontaneously responding the safety risk under thermal abuse conditions. Furthermore, the SRR membrane shows improved resistance to both combustion and high-temperature shrinkage (~2% at 160°C), far outpacing the conventional hydrocarbon-based polymers. This strategy provides a feasible strategy for improving the safety of high-energy-density rechargeable Li batteries without compromising their performance.

RESULTS

Thermal properties of the TPF membrane

Among all P-based flame retardants, we selected DEAP due to its relatively low molar and mass enthalpy of combustion (fig. S1), which is crucial to reducing the heat release during thermal runaway. The ethylenic bond of DEAP (Fig. 2A) makes it possible to bond with a polymer framework (TMPETA; Fig. 2A) to avoid free P-containing species in the electrolyte, which are adverse to the electrochemical performance. We used a simple ultraviolet (UV) curing method to prepare the TPF membrane. In the typical UV-cured polymerization process, the ethylenic bonds of TMPETA/DEAP monomers open and reconnect with each other. Because the TMPETA molecule has three terminal C═C bonds for proceeding with the polymerization reaction, the TMPETA monomers connect to form the cross-linked poly-TMPETA backbone, and the DEAP monomers were grafted onto the backbone as the functional branch. In this way, a cross-linked poly-TMPETA/DEAP is obtained, which physically forms an interpenetrating network with linear PVDF-HFP (no chemical reaction occurs between the two polymers). We further removed any unbonded DEAP by dimethyl carbonate (DMC) washing to eliminate free P-containing species. The TPF polymer shows excellent compatibility with a commercial separator (Fig. 2B). Fourier transform infrared (FTIR) spectrum of TPF (Fig. 2C) shows peaks of P—O—C (~960 and ~1030 cm^{-1}) groups in TPF, as compared with DEAP, while TMPETA does not show the P—O—C peaks. The above results confirm the chemical bonding of DEAP to the polymer backbone by opening the C═C bonds under UV irradiation.

Under thermal abuse conditions, partial bonding of the TPF membrane can break to release P-containing radicals. We calculated the bonding energies of the DEAP/TMPEA by density functional theory (DFT). The bonds in DEAP tend to break at four sites (Fig. 2D), which have bonding energies of 3 to 4 eV, releasing P-containing radicals. As depicted in Fig. 2E, the P-containing radicals [PO]• impede the combustion chain reactions by collisional quenching with highly reactive free radicals (H• and HO•), thus notably alleviating the heat generation. We show the thermal safety and flame-retardant capability of the TPF membrane (in the presence of organic carbonate electrolyte) by combustion test (Fig. 2F and movies S1 to S3), in comparison with commercial PE and TMPETA-PE oxide (PEO) membranes. The PE and TMPETA-PEO membranes show sustained combustion until depletion of organic electrolytes and substantial self-shrinkage. In contrast, after burning with flame, the TPF membrane remains intact without obvious shrinkage and presents a flame-retardant feature. We further compare the shrinkage factor of PE and TPF membranes at different temperatures (Fig. 2G). The PE membrane starts

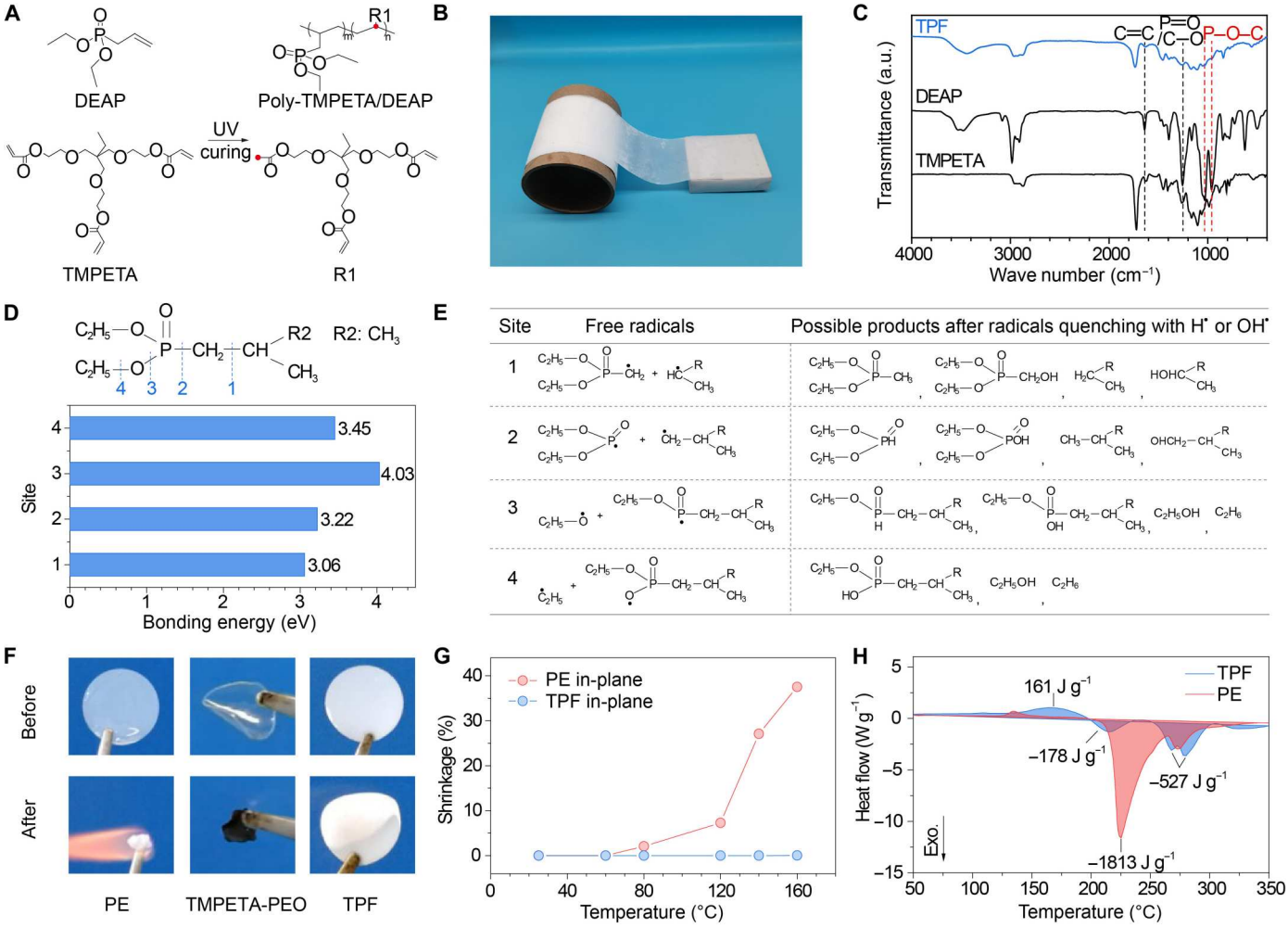

Fig. 2. Structure and thermal stability of the TPF membrane. (**A**) Polymerization of DEAP and TMPETA monomers by ultraviolet (UV) curing. (**B**) Optical image of a roll of TPF-Celgard composite membrane. Photo credit: Ying Zhang, Institute of Chemistry, Chinese Academy of Science. (**C**) Fourier transform infrared (FTIR) spectra of TPF, DEAP, and TMPETA. a.u., arbitrary units. (**D**) Density functional theory (DFT) calculations of bond energy at different sites of the DEAP functional group at 298.15 K. (**E**) Free radicals produced at different sites of the DEAP functional group and possible products from radicals quenching. (**F**) Combustion experiment of polyethylene (PE), TMPETA-PEO (PE oxide), and TPF membranes. Photo credit: Ying Zhang, Institute of Chemistry, Chinese Academy of Science. (**G**) Shrinkage factors of PE and TPF membranes in the temperature range of 20° to 160°C. (**H**) Differential scanning calorimetry (DSC) profiles of a carbonate electrolyte consisting of 1 M $LiPF_6$ in ethylene carbonate (EC)/diethyl carbonate (DEC)/dimethyl carbonate (DMC) (volume ratio: 1:1:1) and charged NCM811 cathode with PE or TPF.

shrinking upon heating to 80°C and contracts by 38% at 160°C, while the TPF shows a much smaller shrinkage, only ~2% at 160°C. This phenomenon could be ascribed to the different polymer structures of PE and TPF. PE is a thermoplastic polymer with a linear structure. Upon heating, PE does not invite intermolecular cross-linking, so that it shows a large yet reversible shrinkage. In contrast, TPF is a thermosetting plastic polymer with a cross-linked structure, which contributes to improved thermal stability to resist shrinkage upon heating. The excellent anti-shrinkage capability of the TPF membrane prevents the possible internal short circuit caused by separator meltdown and reduces the risk of thermal runaway.

We used differential scanning calorimetry (DSC) to examine the thermal abuse tolerance of the electrolyte in a combination with a fully charged $LiNi_{0.8}Co_{0.1}Mn_{0.1}O_2$ (NCM811) electrode, which greatly influences the thermal stability of Li-ion battery. As essential components in Li-ion batteries, the carbonate electrolyte and fully charged NCM811 electrode exhibit exothermic peaks at ~270° and 230°C, respectively (figs. S2 and S3). Their mixture with PE membrane shows an exothermic peak at ~225°C with a total heat release of 1813 J g^{-1} (Fig. 2H). The early occurrence of the exothermic peak is likely due to the participation of the released lattice oxygen in the thermal decomposition of the electrolyte (*29*). After replacing the PE membrane with the TPF membrane, the main exothermic peaks move toward a higher temperature region with a total heat release of 705 J g^{-1}. The exothermic heat is reduced by 60% compared with the case of PE, which will greatly lessen the heat generation in a thermal runaway process.

Electrochemical performance of TPF-based batteries

As a result of the SRR strategy, the thermal safety enhancement is not at the expense of battery performance at room temperature.

Here, the flame-retardant P-contained species (DEAP) are covalently connected with the cross-linked poly-TMPETA skeleton, which effectively eliminates the free P-based flame-retardant additives that are reported detrimental to the interfacial stability of the graphite or Li metal anodes (*27*). Like most electrolytes with P-based flame retardants, the electrolyte with 1 M $LiPF_6$ in the DEAP solvent shows a narrow electrochemical stability window of 1.9 to 4.0 V (versus Li^+/Li), with severe side reactions beyond the voltage range, as evidenced by the linear sweep voltammetry curve (Fig. 3A). In contrast, the TPF without free DEAP presents a wide electrochemical stability window of 0 to 4.6 V (versus Li^+/Li) (Fig. 3A). The wide window ensures stable operation of high-energy Li batteries with multiple anode-cathode combinations, for example, SiO_x-G//NCM811 and Li//$LiCoO_2$.

We conducted x-ray photoelectron spectrum (XPS) to compare the different effects of TPF membrane and DEAP solvent on the electrode interfaces. An electrolyte of 1 M $LiBF_4$ in ethylene carbonate (EC)/diethyl carbonate (DEC)/DMC (volume ratio: 1:1:1) was selected to characterize the P decompositions from DEAP and TPF free of the concern from $LiPF_6$ decompositions. Taking a SiO_x-G anode as an example, the free DEAP molecules decompose into phosphonate and phosphate derivatives on the SiO_x-G surface and even PC_xH_y at an etching depth of 40 nm (fig. S4A), indicating a continuous decomposition of DEAP during the electrochemical process. In contrast, the SiO_x-G electrode in contact with TPF shows a much lower content of P-containing species (fig. S4, B and C), which demonstrates negligible decomposition of the grafted DEAP of TPF. Instead, the SiO_x-G/DEAP interface shows the $BF_3[PO(C_xH_y)_3]$ and LiF as the decomposition products of $LiBF_4$ and DEAP. The SiO_x-G/TPF interface shows more F-rich components ($LiBF_xO_y$ and LiF) derived solely from the $LiBF_4$ salt than the SiO_x-G/DEAP interface (fig. S5), which are critical solid electrolyte interphase (SEI) components to passivate the anode surface (*30*, *31*). The results also agree with the differences in atomic percentage variations of Li, O, P, and F along the etching depth range of 0 to 40 nm (fig. S6). On the cathode side (using NCM811 as an example), the chemical compositions at the NCM811/TPF interface are consistent with those at the NCM811/

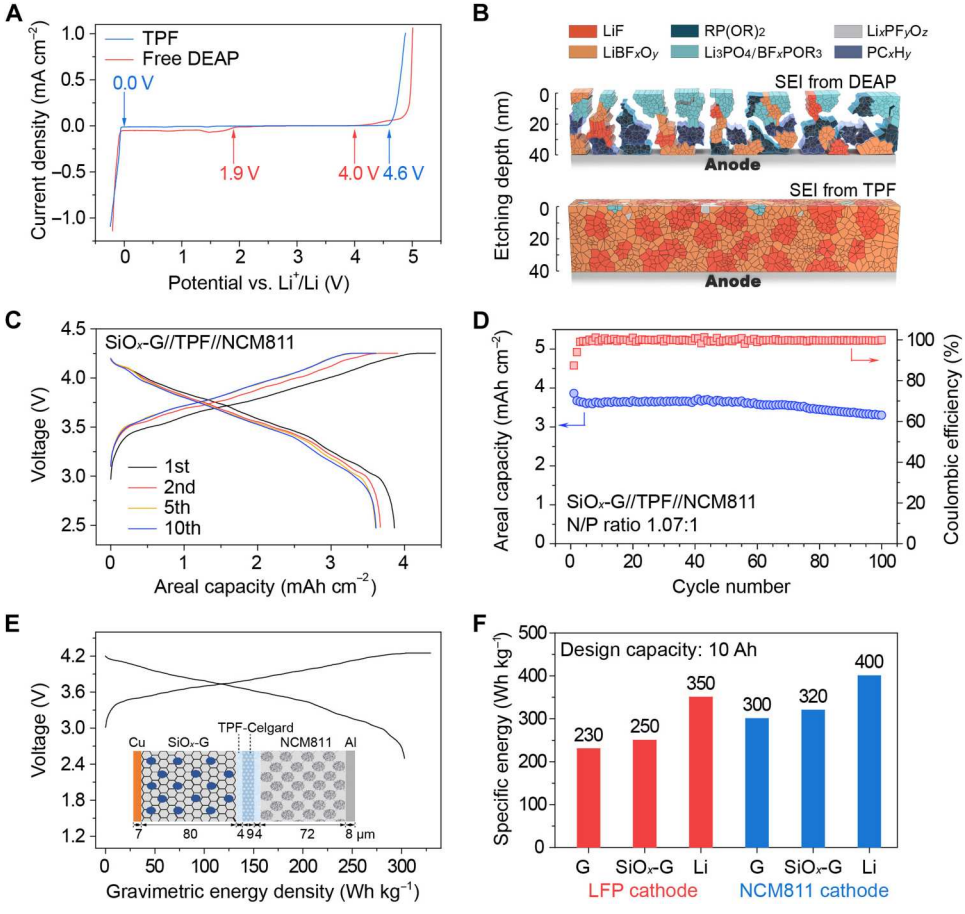

Fig. 3. TPF-based high-performance Li-ion batteries at room temperature. (**A**) Electrochemical stability window of TPF in comparison with an electrolyte containing free DEAP measured by linear sweep voltammetry at 0.1 mV/s. (**B**) Schematic illustration showing the SEI structure on the surface of different SiO_x-graphite (SiO_x-G) electrodes in contact with the free DEAP solvent (top panel) and TPF (bottom panel). (**C** and **D**) Typical charge-discharge voltage profiles and cycling performance of the SiO_x-G//TPF//NCM811 cell at 0.2 C. N/P, negative/positive capacity ratio. (**E**) Gravimetric energy density of a SiO_x-G//TPF-Celgard//NCM811 cell (inset: schematic of the SiO_x-G//TPF-Celgard//NCM811 cell with the dimensions of different components). Refer to table S1 and fig. S16 for more details. (**F**) The projected energy density of G//LFP, SiO_x-G//LFP, Li//LFP, G//NCM811, SiO_x-G//NCM811, and Li//NCM811 pouch cells with a design capacity of 10 Ah based on the TPF-Celgard membranes. Refer to tables S2 to S4 for the detailed cell parameters.

Celgard interface in the control experiment (fig. S7), which confirms the electrochemical compatibility of TPF with high-voltage cathode materials. Thus, TPF circumvents the commonly observed decomposition of P-based flame-retardants while forming an F-rich SEI layer on the anode and a stable interface on the cathode (Fig. 3B), compatible with high-energy-density batteries.

We demonstrate TPF-based high-energy batteries using SiO_x-G//TPF//NCM811 full cells with a high mass loading (22 mg cm^{-2}) of active materials in the cathode and a low negative/positive (N/P) ratio (1.07) based on the specific capacities of electrodes in Li half cells (fig. S8). In this cell, TPF refers to a 44-μm-thick pure TPF membrane (fig. S9). At room temperature, the TPF membrane filled with 20 μl of carbonate electrolyte shows a high ionic conductivity of 2.8×10^{-3} S cm^{-1} (fig. S10). The SiO_x-G//TPF//NCM811 full cell exhibits stable cycling performance at 0.2 C with a high reversible capacity of 3.9 mAh cm^{-2}, an average Coulombic efficiency of 99.6%, and a high capacity retention of 91.4% (versus second cycle) after 100 cycles (Fig. 3, C and D). To verify the practicality of TPF, a 0.68-Ah SiO_x-G//TPF//NCM811 pouch cell was assembled. It delivers a reversible capacity of 0.5 Ah in the first cycle, an average Coulombic efficiency of 99.96% (excluding the first cycle), and a high capacity retention of 97% (excluding the first cycle) after 60 cycles (fig. S11). Such a stable battery performance can hardly be achieved by using free P-containing flame-retardant solvents. For example, the capacity of the cell using DEAP as the electrolyte solvent (fig. S12) declines to zero after the initial charge due to the poor cathodic stability against the SiO_x-G anode. The TPF membrane is also compatible with the use of the Li-metal anode. A Li//TPF-Celgard//$LiCoO_2$ cell demonstrates a high capacity retention of 80.4% for over 500 cycles (fig. S13). These results prove that the covalent bond between the DEAP molecules and the polymer skeleton notably improves the interfacial stability of the P-containing species against anodes (graphite-based anodes, Li metal, etc.) as well as the high-voltage cathode materials (NCM811) for long-term operation of batteries.

The TPF polymer also shows favorable compatibility with large-scale battery manufacture. Because of the excellent wettability of TPF precursor with the commercial separator and the simple UV

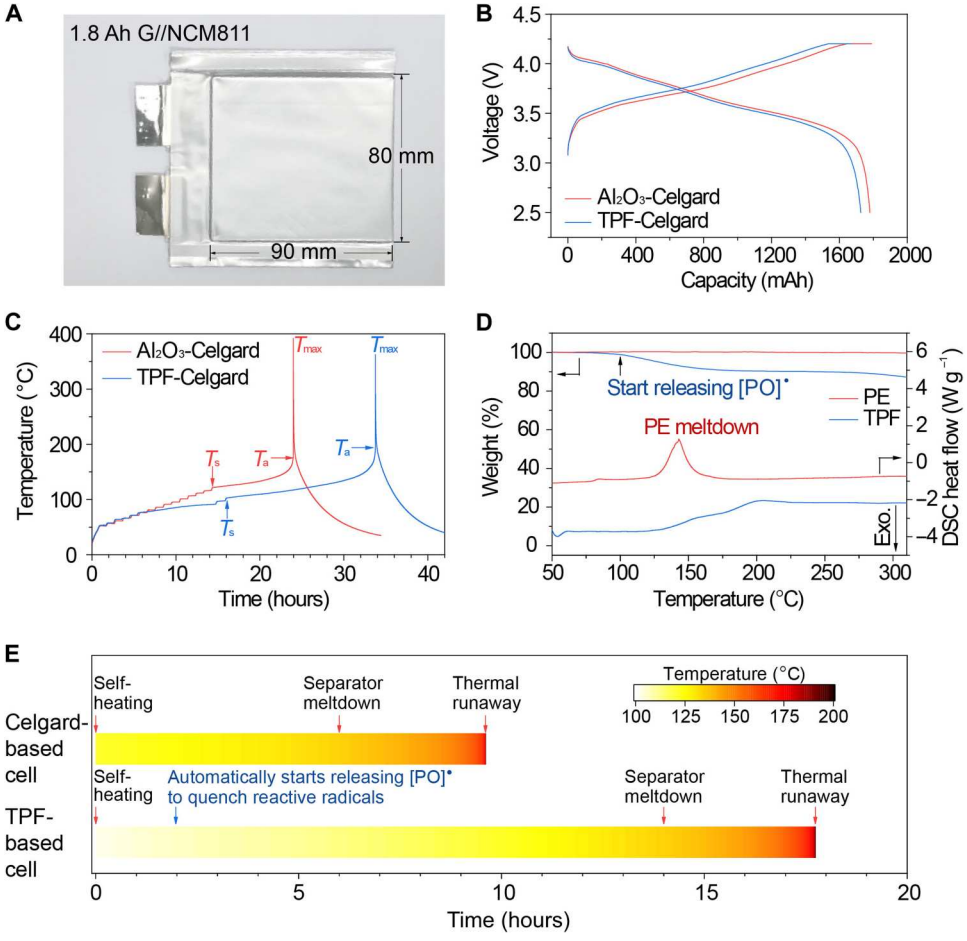

Fig. 4. Thermal stability of pouch cells. (**A**) Optical image of a G//NCM811 pouch cell. Photo credit: Ying Zhang, Institute of Chemistry, Chinese Academy of Science. (**B**) Typical charge-discharge profiles of the G//NCM811 pouch cells using commercial Al_2O_3-Celgard and TPF-Celgard separators. (**C**) ARC profiles of the charged pouch cells, which record the time and temperature at the occurrence of thermal runaway. For a clear comparison, both of the profiles adopt the same scale. T_s is defined as the self-heating temperature, T_a is defined as the heating accelerating temperature during the thermal runaway process when dT/dt is 1°C s^{-1} (the dT/dt-T and dT/dt-t curves are shown in fig. S17) (*30*, *37*), and T_{max} is defined as the maximum temperature during thermal runaway. (**D**) Thermogravimetry (TG) and DSC profiles of PE and TPF membranes. (**E**) Timeline of thermal incidents in the 1.8-Ah G//NCM811 pouch cells loaded with different membranes.

curing process (fig. S14), the fabrication of the composite membrane can be integrated into the conventional roll-to-roll manufacturing process, which includes steps of UV curing, residue removal by solvent washing (optional), and drying (fig. S15), for scaled-up production of the safety-enhanced separators. With thin (~4 μm) and low-density (0.6 g cm^{-3}) TPF coatings on both sides of a Celgard separator (~9 μm) (fig. S16A), the use of the TPF-Celgard composite membrane in rechargeable Li batteries contributes more to the cell safety yet less to the cell weight (that lowers the energy output). We show a SiO_x-G//TPF-Celgard//NCM811 cell assembled with single-side-coated electrodes (SiO_x-G with a thickness of 80 μm and NCM811 with a thickness of 70 μm; fig. S16, B and C) delivering a specific energy of 303 Wh kg^{-1} and a volumetric energy density of 852 Wh $liter^{-1}$ (based on the total mass of battery components excluding the package; Fig. 3E and table S1). By using the TPF-Celgard composite, we anticipate safer and high-energy-density batteries with other anode-cathode combinations in 10-Ah pouch cells (e.g., G//lithium iron phosphate (LFP), SiO_x-G//LFP, Li//LFP, G//NCM811, SiO_x-G//NCM811, and Li//NCM811 cells according to Fig. 3F and tables S2 to S4).

The safety performance of TPF-based pouch cells

We demonstrate the safety enhancement of the TPF-modified Celgard separator in 1.8-Ah G//NCM811 pouch cells (Fig. 4A) in comparison with pouch cells using a commercial Al_2O_3-Celgard separator. The pouch cells were assembled with the TPF-Celgard or Al_2O_3-Celgard membranes with total capacities of ~1.8 Ah (Fig. 4B). We charged the pouch cell to 4.2 V and then maintained it at 4.2 V for 30 min to achieve a fully charged state (which is also the most hazardous state) and then used accelerating rate calorimeter (ARC) measurement to precisely track the temperature change inside the fully charged pouch cells in an adiabatic environment (Fig. 4C, Table 1, and fig. S17). Both cells start self-heating at roughly 100°C (self-heating temperature, T_s) after being externally heated for about 15 hours. The control cell (using Al_2O_3-Celgard separator) shows a heating acceleration (T_a; when dT/dt = 1°C s^{-1}) after 8.9 hours of self-heating and reached the maximum temperature (T_{max}) and catastrophic thermal runaway shortly. In contrast, the TPF-Celgard membrane reduces the T_{max} by about 30°C compared with the control sample. Moreover, TPF-Celgard remarkably delays the heating acceleration by 100%, giving a 17.8-hour time window from self-heating to catastrophic thermal runaway (Table 1). We further verified the delayed thermal runaway effect of TPF by COMSOL Multiphysics, considering the heat flux influence at ambient temperature (see Materials and Methods and fig. S18 for simulation details). Compared with the Al_2O_3-Celgard cell, the TPF-Celgard cell substantially increases the time before the exponential increase of heat flow from 4.7 to 10 hours (fig. S19), mitigating thermal runaway issues in the cell. Thus, the intervention of P-containing radicals has a positive effect in suppressing battery thermal accumulation and delays the occurrence of thermal runaway.

The safety enhancement effect of TPF is realized by its SRR at the abusive temperature. According to the thermogravimetry (TG) and DSC analyses (Fig. 4D and fig. S20), the TPF membrane starts to lose weight (releasing P-containing radicals, $[PO]^•$) at ~87°C, which is about the self-heating temperature of the cells. Throughout the cell self-heating process (100° to 200°C), the TPF membrane continuously releases $[PO]^•$ radicals, which scavenge the highly reactive free radicals ($H^•$, $HO^•$, and $O^•$) produced from thermal decomposition of organic electrolytes and high-nickel cathodes at elevated temperatures. In contrast, PE shows a sharp peak at ~140°C (Fig. 4D), indicating the meltdown of PE. The PE meltdown would induce an internal short circuit, which contributes to further heat generation and aggravates the thermal runaway.

On the basis of the ARC test (Fig. 4C) and thermal analyses (Fig. 4D), we compare the timeline of thermal incidents (t) in the 1.8-Ah G//NCM811 pouch cells using commercial Al_2O_3-Celgard and TPF-Celgard membranes, starting from the self-heating of each cell (Fig. 4E). The Al_2O_3-Celgard cell undergoes separator meltdown at t = ~6 hours and catastrophic thermal runaway at t = 8.9 hours. With the TPF-Celgard membrane, the TPF starts releasing $[PO]^•$ at t = ~2 hours (~90°C) after the cell self-heating, which is an automatic risk response and continues throughout the whole process. The $[PO]^•$ radicals detached from the polymer quench the active free radicals ($H^•$ and $HO^•$) as discussed in Fig. 2E to alleviate the thermal runaway. As a result, the occurrence of separator meltdown and catastrophic thermal runaway is substantially postponed, giving a critical 17.8-hour time window for safety management. More attractively, as the risk response only occurs in abusive conditions (>90°C), the TPF membrane still guarantees the stable electrochemical performance of the cells under normal operations, realizing the SRR batteries.

DISCUSSION

In summary, we propose an SRR strategy to resolve the long-existing conflict between energy density and the safety of energy storage systems. Instead of the common practice of adding P-containing electrolyte additives, which are flame-retarding but are harmful to the battery performance, we grafted phosphorus-containing functional groups onto a hydrocarbon-based polymer skeleton as an SRR membrane. The SRR membrane does not generate free P-containing species at room temperature, thus guaranteeing the high-performance operation of batteries, as evidenced by a SiO_x-G//NCM811 battery with a high reversible areal capacity of 3.9 mAh cm^{-2}, an average Coulombic efficiency of 99.6%, and a high capacity retention of 91.4% after 100 cycles. As a safety-enhancing separator, the SRR membrane has a much smaller shrinkage upon heating (2% at 160°C) and lower heat generation compared with

Table 1. T_s, T_a, and T_{max} of the pouch cells using TPF-Celgard and Al_2O_3-Celgard membranes based on ARC data.

Cell	T_s (°C)	T_a (°C)	T_{max} (°C)	Time window (T_s to T_{max}) (hours)
Al_2O_3-Celgard	123	177	392	8.9
TPF-Celgard	102	193	363	17.8

commercial PE. In thermal abusing conditions, it automatically releases P-containing radicals at >90°C to impede the combustion chain reactions of highly reactive $H^{\bullet}$ and $HO^{\bullet}$ free radicals generated at elevated temperatures. As a result, the SRR membrane greatly delays the thermal runaway by 100% (~9 hours) compared with the commercial separators, winning a critical safety responding time before the catastrophic thermal incidence. The SRR strategy provides a practical way to breach the dilemmas of high energy density or high safety in energy storage devices, bringing the possibility for safe energy utilization.

MATERIALS AND METHODS

Material fabrication and batteries

The TPF membrane was fabricated by photocuring the precursor mixture. TMPETA ($C_{20}O_9H_{22}$; Aladdin Inc.) and DEAP ($C_7H_{15}PO_3$; Energy Chemical Inc.) were first mixed with a molar ratio of 2:1.3. Photoinitiator (2-hydroxy-2-methyl-1-phenyl-1-propanone; Sigma-Aldrich Inc.) was added into the above TMPETA-DEAP solution with a dosage of 11 μL mL^{-1}. Then, PVDF-HFP (Sigma-Aldrich Inc.) anhydrous dimethyl sulfoxide (Alfa Aesar. Inc.) solution was prepared with a concentration of 55 mg mL^{-1}. The precursor solution was prepared by mixing the TMPETA-DEAP solution and PVDF-HFP solution with a volume ratio of 1:1. Last, the TPF membrane was prepared by casting the precursor onto a glass panel and curing it for 8 min under UV light (power: 2000 W). Before material characterizations and application in the cells, the TPF membrane was washed with DMC solvent to remove the residual DEAP monomers and dried in the glove box. The TMPETA/DEAP molar ratio in TPF was 2:1 confirmed by the XPS analysis. The fabrication process of TMPETA-PEO used as the control membrane was reported previously (*32*).

Full cell configurations with NCM811 cathodes, TPF membrane, and SiO_x-G anodes were adopted to examine the electrochemical stability of TPF in 2032-type coin cells. The TPF membrane was composited with 20 μL of electrolytes of 1 M $LiPF_6$ in EC/DEC/DMC (v/v 1:1:1) with 5% fluoroethylene carbonate. Both the cathodes and anodes were provided by Beijing IAmetal New Energy Technology Co. Ltd. To investigate the influence of free-state DEAP, 1 M $LiPF_6$ was dissolved in the DEAP solvent to fabricate the $LiPF_6$-DEAP electrolyte. To probe its versatility, the TPF-Celgard composites were used in the 2032-type Li//LCO cells and pouch-type SiO_x-G//NCM811 cells. The galvanostatic cycling test was conducted on the LAND system (LANHE Inc. CT2001A). The ionic conductivity and electrochemical window of TPF polymer electrolytes were respectively conducted in symmetric stainless steel cells and Li//stainless steel cells with the electrochemical workstation (Princeton Inc.).

Material characterization

FTIR spectra were recorded on a TENSOR 27 FTIR spectrometer (Bruker Inc.) to identify the functional groups in TPF. Morphologies of TPF membranes were characterized by field-emission scanning electron microscopy (Hitachi Inc., S-4800). The XPS data of both cathodes and anodes were collected from the ESCALAB250XI (Thermo Fisher Scientific Inc.).

Battery safety evaluation

TG (STA 449F3 Jupiter) and DSC (NETZSCH Inc.) tests were performed with a scan rate of 10°C min^{-1}. Before the DSC test, the cathodes were charged to 4.3 V. The cathode composites were scraped from Al foil via a blade. The carbonate electrolyte (1.2 μL mg^{-1} based on the mass of active material) and TPF membrane (0.25 mg mg^{-1}) were mixed and sealed in a 100-μL high-pressure crucible with a gold-plated surface. The above operation processes were conducted in an Ar-filled glove box. ARC tests (conducted by China Automotive Battery Research Inovativate Co. Ltd.) were performed on the 1.8-Ah graphite//NCM811 pouch cells with an EV^+-ARC system (Thermal Hazard Technology Inc.). During the test, the cells were heated in a cylindrical calorimeter. The temperature begins at 50°C with a heating step of 5°C and a temperature sensitivity of 0.02°C min^{-1} in an adiabatic environment. If the increased rate of cell temperature exceeds 0.02°C min^{-1}, the self-heating of the cell begins; in the meantime, the ARC system stops heating the cell. The separator (SC12-S3-J) used in the control experiment was purchased from Hebei Gellec New Energy Science & Technology Joint Stock Co. Ltd.

DFT calculations

All the calculations were performed by using the Gaussian 09 package (*33*). Minimum energy geometries for solvent molecules were optimized by the dispersion-corrected density functional method M06-2x-D3 (*34*) with the 6-311G(d) basis set (*35*, *36*) for all atoms. Normal vibrational mode analysis at the same level of theory was performed to confirm the optimized structures are minima (zero imaginary frequency) and to obtain the thermal enthalpies. The lowest energy conformers for each solvent were used in estimating the enthalpy change of the combustion process. To reveal the possible bond-breaking sites of the DEAP molecule, the Gibbs free energy of bond cleavage was used to qualitatively estimate such possibility, as shown in the equation below.

$$\Delta G_{break} = G_{frag.1} + G_{frag.2} - G_{mol.} \quad (1)$$

where ΔG_{break} is the bond cleavage free energy. $G_{mol.}$, $G_{frag.1}$, and $G_{frag.2}$ are the thermal corrected Gibbs free energy of the molecule and the radical fragments at 298.15 K, respectively. The molecule and radicals were optimized with B3LYP functional, and the basis set of 6-311+G(2df,p) was chosen. Frequency analysis was further conducted at the same calculation level to confirm the systems have reached optimal configurations. To gain a more accurate description of reaction energy, the electron energy of the optimized systems is recalculated with the M06-2x functional and def2-TZVP basis set. Thermal corrections to the Gibbs free energy were obtained through the frequency analysis process.

COMSOL Multiphysics simulations

The simulation work was carried out on a COMSOL Multiphysics 5.5 software using the physics module of "Heat transfer in solid" with natural convection boundary conditions. Here, the battery pack is simplified as the Al thin slice with a thickness of 2 mm, and the surface area is defined as 8 cm by 9 cm. The heat flux below the Al slice stemmed from the simulation result based on the segment of the ARC time-temperature curve (Fig. 4C) from T_s to T_a (fig. S18). The governing equation of energy conservation

is shown as Eq. 2

$$\rho c_p \frac{\partial T}{\partial t} = \nabla \cdot (k \nabla T) \quad (2)$$

The boundary conditions applied at the upper and lower surface are set as below. Notably, the heat flux through the four side surfaces is negligible for the tiny heat transfer area. Effects of natural convection heat transfer at the upper and lower surface are evaluated by Eqs. 3 to 5

$$\text{For upper surface}: Nu = 0.54 Ra^{0.25} \quad (3)$$

$$\text{For lower surface}: Nu = 0.27 Ra^{0.25} \quad (4)$$

$$Ra = Pr \cdot Gr = \frac{\nu}{\alpha} \frac{g \beta L^3 \Delta T}{\nu^2} \quad (5)$$

The heat transfer coefficient of natural convection is solved by Eq. 6

$$h = \frac{k_g}{L} Nu \quad (6)$$

The heat flux through the upper surface and the lower surface are evaluated by Eqs. 7 and 8

$$\text{For upper surface}: -k_g \nabla T = -h(T - T_{sur}) + N_R \quad (7)$$

$$\text{For lower surface}: -k_g \nabla T = -h(T - T_{sur}) + N_T + N_R \quad (8)$$

The heat radiation flux is expressed as Eq. 9

$$N_R = \varepsilon \sigma (T_{sur}^4 - T^4) \quad (9)$$

The symbols, their physical meanings, units, and physical properties used in Eqs. 2 to 9 are displayed in tables S5 and S6.

Supplementary Materials

This PDF file includes:
Figs. S1 to S20
Tables S1 to S6

Other Supplementary Material for this manuscript includes the following:
Movies S1 to S3

REFERENCES AND NOTES

1. J. W. Choi, D. Aurbach, Promise and reality of post-lithium-ion batteries with high energy densities. *Nat. Rev. Mater.* **1**, 16013 (2016).
2. J. Lu, Z. Chen, Z. Ma, F. Pan, L. A. Curtiss, K. Amine, The role of nanotechnology in the development of battery materials for electric vehicles. *Nat. Nanotechnol.* **11**, 1031–1038 (2016).
3. W. Li, E. M. Erickson, A. Manthiram, High-nickel layered oxide cathodes for lithium-based automotive batteries. *Nat. Energy* **5**, 26–34 (2020).
4. T. Liu, L. Lin, X. Bi, L. Tian, K. Yang, J. Liu, M. Li, Z. Chen, J. Lu, K. Amine, K. Xu, F. Pan, In situ quantification of interphasial chemistry in Li-ion battery. *Nat. Nanotechnol.* **14**, 50–56 (2019).
5. H. Sun, J. Zhu, D. Baumann, L. Peng, Y. Xu, I. Shakir, Y. Huang, X. Duan, Hierarchical 3D electrodes for electrochemical energy storage. *Nat. Rev. Mater.* **4**, 45–60 (2019).
6. H. Liu, Z. Zhu, Q. Yan, S. Yu, X. He, Y. Chen, R. Zhang, L. Ma, T. Liu, M. Li, R. Lin, Y. Chen, Y. Li, X. Xing, Y. Choi, L. Gao, H. S. Y. Cho, K. An, J. Feng, R. Kostecki, K. Amine, T. Wu, J. Lu, H. L. Xin, S. P. Ong, P. Liu, A disordered rock salt anode for fast-charging lithium-ion batteries. *Nature* **585**, 63–67 (2020).
7. X. Han, Y. Gong, K. Fu, X. He, G. T. Hitz, J. Dai, A. Pearse, B. Liu, H. Wang, G. Rubloff, Y. Mo, V. Thangadurai, E. D. Wachsman, L. Hu, Negating interfacial impedance in garnet-based solid-state Li metal batteries. *Nat. Mater.* **16**, 572–579 (2017).
8. Y. Li, W. Zhou, X. Chen, X. Lü, Z. Cui, S. Xin, L. Xue, Q. Jia, J. B. Goodenough, Mastering the interface for advanced all-solid-state lithium rechargeable batteries. *Proc. Natl. Acad. Sci. U.S.A.* **113**, 13313–13317 (2016).
9. J. Hao, F. Yang, S. Zhang, H. He, G. Xia, Y. Liu, C. Didier, T. Liu, W. K. Pang, V. K. Peterson, J. Lu, Z. Guo, Designing a hybrid electrode toward high energy density with a staged Li+ and PF6− deintercalation/intercalation mechanism. *Proc. Natl. Acad. Sci. U.S.A.* **117**, 2815–2823 (2020).
10. K. Liu, Y. Liu, D. Lin, A. Pei, Y. Cui, Materials for lithium-ion battery safety. *Sci. Adv.* **4**, eaas9820 (2018).
11. L. Hu, K. Xu, Nonflammable electrolyte enhances battery safety. *Proc. Natl. Acad. Sci. U.S.A.* **111**, 3205–3206 (2014).
12. Q. Zheng, Y. Yamada, R. Shang, S. Ko, Y. Y. Lee, K. Kim, E. Nakamura, A. Yamada, A cyclic phosphate-based battery electrolyte for high voltage and safe operation. *Nat. Energy* **5**, 291–298 (2020).
13. Y. Li, H. Pu, Y. Wei, Polypropylene/polyethylene multilayer separators with enhanced thermal stability for lithium-ion battery via multilayer coextrusion. *Electrochim. Acta* **264**, 140–149 (2018).
14. T. Kawamura, A. Kimura, M. Egashira, S. Okada, J.-I. Yamaki, Thermal stability of alkyl carbonate mixed-solvent electrolytes for lithium ion cells. *J. Power Sources* **104**, 260–264 (2002).
15. G. Nagasubramanian, K. Fenton, Reducing Li-ion safety hazards through use of non-flammable solvents and recent work at Sandia National Laboratories. *Electrochim. Acta* **101**, 3–10 (2013).
16. H.-J. Noh, S. Youn, C. S. Yoon, Y.-K. Sun, Comparison of the structural and electrochemical properties of layered Li[$Ni_xCo_yMn_z$]O2 (x = 1/3, 0.5, 0.6, 0.7, 0.8 and 0.85) cathode material for lithium-ion batteries. *J. Power Sources* **233**, 121–130 (2013).
17. Z. Zhang, Y. Shao, B. Lotsch, Y. S. Hu, H. Li, J. Janek, L. F. Nazar, C. W. Nan, J. Maier, M. Armand, L. Chen, New horizons for inorganic solid state ion conductors. *Energ. Environ. Sci.* **11**, 1945–1976 (2018).
18. J. Xu, X. Ji, J. Zhang, C. Yang, P. Wang, S. Liu, K. Ludwig, F. Chen, P. Kofinas, C. Wang, Aqueous electrolyte design for super-stable 2.5 V LiMn2O4 || Li4Ti5O12 pouch cells. *Nat. Energy* **7**, 186–193 (2022).
19. H. Zhang, X. Liu, H. Li, I. Hasa, S. Passerini, Challenges and strategies for high-energy aqueous electrolyte rechargeable batteries. *Angew. Chem. Int. Ed.* **60**, 598–616 (2021).
20. X. Wang, E. Yasukawa, S. Kasuya, Nonflammable trimethyl phosphate solvent-containing electrolytes for lithium-ion batteries: I. Fundamental properties. *J. Electrochem. Soc.* **148**, A1058 (2001).
21. T. Dagger, B. R. Rad, F. M. Schappacher, M. Winter, Comparative performance evaluation of flame retardant additives for lithium ion batteries – I. Safety, chemical and electrochemical stabilities. *Energy Technol.* **6**, 2011–2022 (2018).
22. A. B. Morgan, J. M. Tour, Synthesis and testing of nonhalogenated alkyne-containing flame-retarding polymer additives. *Macromolecules* **31**, 2857–2865 (1998).
23. J. M. Catala, J. Brossas, Synthesis of fire retardant polymers without halogens. *Prog. Org. Coat.* **22**, 69–82 (1993).
24. E.-G. Shim, T.-H. Nam, J.-G. Kim, H.-S. Kim, S.-I. Moon, Electrochemical performance of lithium-ion batteries with triphenylphosphate as a flame-retardant additive. *J. Power Sources* **172**, 919–924 (2007).
25. B. S. Lalia, N. Yoshimoto, M. Egashira, M. Morita, A mixture of triethylphosphate and ethylene carbonate as a safe additive for ionic liquid-based electrolytes of lithium ion batteries. *J. Power Sources* **195**, 7426–7431 (2010).
26. Y. E. Hyung, D. R. Vissers, K. Amine, Flame-retardant additives for lithium-ion batteries. *J. Power Sources* **119-121**, 383–387 (2003).
27. K. Xu, M. S. Ding, S. Zhang, J. L. Allen, T. R. Jow, An attempt to formulate nonflammable lithium ion electrolytes with alkyl phosphates and phosphazenes. *J. Electrochem. Soc.* **149**, A622–A626 (2002).
28. T. Shiga, Y. Kato, H. Kondo, C.-a. Okuda, Self-extinguishing electrolytes using fluorinated alkyl phosphates for lithium batteries. *J. Mater. Chem. A* **5**, 5156–5162 (2017).
29. M. Dixit, B. Markovsky, F. Schipper, D. Aurbach, D. T. Major, Origin of structural degradation during cycling and low thermal stability of Ni-rich layered transition metal-based electrode materials. *J. Phys. Chem. C* **121**, 22628–22636 (2017).
30. X. Fan, X. Ji, F. Han, J. Yue, J. Chen, L. Chen, T. Deng, J. Jiang, C. Wang, Fluorinated solid electrolyte interphase enables highly reversible solid-state Li metal battery. *Sci. Adv.* **4**, eaau9245 (2018).

31. H. Duan, W. P. Chen, M. Fan, W. P. Wang, L. Yu, S. J. Tan, X. Chen, Q. Zhang, S. Xin, L. J. Wan, Y. G. Guo, Building an air stable and lithium deposition regulable garnet interface from moderate-temperature conversion chemistry. *Angew. Chem. Int. Ed.* **59**, 12069–12075 (2020).
32. X.-X. Zeng, Y. X. Yin, N. W. Li, W. C. du, Y. G. Guo, L. J. Wan, Reshaping lithium plating/stripping behavior via bifunctional polymer electrolyte for room-temperature solid Li metal batteries. *J. Am. Chem. Soc.* **138**, 15825–15828 (2016).
33. M. Frisch, G. Trucks, H. Schlegel, G. Scuseria, M. Robb, J. Cheeseman, G. Scalmani, V. Barone, B. Mennucci, G. Petersson, *Gaussian 09* (Gaussian, Inc., 2009).
34. Y. Zhao, D. G. Truhlar, The M06 suite of density functionals for main group thermochemistry, thermochemical kinetics, noncovalent interactions, excited states, and transition elements: Two new functionals and systematic testing of four M06-class functionals and 12 other functionals. *Theor. Chem. Acc.* **120**, 215–241 (2008).
35. R. Kriihnan, J. Binkky, R. Sceger, J. Pople, Self-consistent molecular orbital methods. XX. A basis set for correlated wave-functions. *J. Chem. Phys* **72**, 650–654 (1980).
36. A. D. McLean, G. S. Chandler, Contracted Gaussian basis sets for molecular calculations. I. Second row atoms, Z=11–18. *J. Chem. Phys.* **72**, 5639–5648 (1980).
37. J. Hou, L. Lu, L. Wang, A. Ohma, D. Ren, X. Feng, Y. Li, Y. Li, I. Ootani, X. Han, W. Ren, X. He, Y. Nitta, M. Ouyang, Thermal runaway of lithium-ion batteries employing LiN(SO2F)2-based concentrated electrolytes. *Nat. Commun.* **11**, 5100 (2020).

Acknowledgments

Funding: This work was supported by the National Key R&D Program of China (grant no. 2021YFB2500300), the Basic Science Center Project of Natural Science Foundation of China (grant no. 51788104), Chinese Academy of Sciences (CAS) Project for Young Scientists in Basic Research (grant no. YSBR-058), the National Natural Science Foundation of China (grant nos. 22005316 and 21975266), the Young Elite Scientist Sponsorship Program by CAST (2022QNRC001), the Beijing Natural Science Foundation (grant no. JQ22005), and the "Transformational Technologies for Clean Energy and Demonstration," Strategic Priority Research Program of CAS (grant no. XDA21070300).

Author contributions: Ying Z., S.X., Y.-G.G., and C.B. conceived the original concept and experiments. Ying Z., Y.-H.W., and X.-T.L. carried out the fabrication and performed the material characterizations and electrochemical measurements. X.-D.Z., W.-P.W., Yu Z., and G.L. assisted in the pouch cell assembling and electrochemical measurements. L.Y. and X.-T.L. performed the first-principles calculations. Ying Z., C.Y., S.X., and Y.-G.G. wrote the paper. All authors contributed to discussing the results and commenting on the manuscript.

Competing interests: The authors declare that they have no competing interests.

Data and materials availability: All data needed to evaluate the conclusions in the paper are present in the paper and/or the Supplementary Materials.

Submitted 29 August 2022
Accepted 4 January 2023
Published 1 February 2023
10.1126/sciadv.ade5802